PERSPECTIVE

Check for updates

Copper-based catalysts for CO_2 hydrogenation: a perspective on active sites

Yun-Fei Shi,[a] Sicong Ma [ID] *[b] and Zhi-Pan Liu [ID] *[ab]

CO_2 hydrogenation is regarded as a revolutionized field in heterogeneous catalysis, not only mitigating environmental problems caused by greenhouse gases but also producing valuable chemicals. This Perspective, going over both theoretical and experimental advances, aims to bridge Cu-based catalyst structures, the most important type of CO_2 hydrogenation catalyst, and their catalysis applications with varied activity and selectivity. We provide a systematic overview of the catalytic active sites, the reaction mechanism, and their impact on the reaction selectivity, stability, and activity for CO_2 hydrogenation. There is a particular focus on the nature of the industrial $Cu/ZnO/Al_2O_3$ catalyst, where a large volume of literature is available exploring the reaction energetics on the possible reaction sites, including Cu metal, CuZn alloy, and ZnO_xH_y overlayers. The recent advances in designing better catalytic active sites, such as the Cu single-atom catalyst, supported Cu cluster catalyst, and bimetallic Cu–M, are then followed to illustrate how the activity and selectivity vary upon changing the active sites. Our perspectives on the future research directions are finally provided, which should benefit the understanding of complex catalytic active sites and the design of better CO_2 hydrogenation catalysts.

Broader context

CO_2 hydrogenation is regarded as a revolutionized field in heterogeneous catalysis, not only mitigating environmental problems caused by greenhouse gas but also producing valuable chemicals. This Perspective, going over both theoretical and experimental advances, aims to bridge Cu-based catalyst structures, the most important type of CO_2 hydrogenation catalyst, and their catalysis applications with varied activity and selectivity. We believe that this Perspective can arouse the interest of researchers in related fields and provide some directions for the future research in energy and environmental catalysis.

[a] Collaborative Innovation Center of Chemistry for Energy Material, Shanghai Key Laboratory of Molecular Catalysis and Innovative Materials, Key Laboratory of Computational Physical Science, Department of Chemistry, Fudan University, Shanghai 200433, China. E-mail: zpliu@fudan.edu.cn

[b] Key Laboratory of Synthetic and Self-Assembly Chemistry for Organic Functional Molecules, Shanghai Institute of Organic Chemistry, Chinese Academy of Sciences, Shanghai 200032, China. E-mail: scma@mail.sioc.ac.cn

Yun-Fei Shi graduated from Fudan University in 2019. He is currently doing a PhD degree at Fudan University under the supervision of Prof. Zhi-Pan Liu. His research interests include reaction mechanisms of heterogeneous catalysis and machine learning accelerated automated reaction network exploration.

Yun-Fei Shi

Sicong Ma graduated from the China University of Petroleum (Beijing, China). He received his PhD degree in 2019 at Fudan University under the supervision of Prof. Zhi-Pan Liu. He then continued to stay in Fudan University to carry out post-doctoral research. In 2021 he joined the Shanghai Institute of Organic Chemistry, Chinese Academy of Sciences, where he currently holds a position as an assistant research fellow. His current research interests are mainly focused on the machine learning applications in constructing the homogeneous/heterogeneous catalyst database (e.g. zeolite-related database and phosphine ligand database).

Sicong Ma

1. Introduction

The conversion of carbon dioxide (CO_2) into value-added products *via* heterogeneous catalysis is a promising approach to reducing greenhouse gas emissions with great economic benefits. To date, the hydrogenation of CO_2 and CO mixed gas has already been realized in industry through the low-pressure methanol synthesis process with a Cu-based catalyst, *i.e.* a Cu/ZnO/Al$_2$O$_3$ (CZA) catalyst.[1,2] The global CH_3OH production *via* this technology is massive, reaching 106.89 million metric tons in 2021.[3] This industrial achievement demonstrates the great value of CO_2 conversion in making renewable fuels and chemical compounds. In recent years, significant efforts have been devoted to developing new types of catalysts for CO_2 hydrogenation (without the presence of CO), where the Cu element continues to play a pivotal role in these endeavors. This Perspective focuses on the recent theoretical and experimental advances in the structural characteristics of Cu-based catalysts and their linkages to the product selectivity in CO_2 hydrogenation from a fundamental point of view.

The industrial CZA catalyst serves as a textbook example for understanding how CO_2 is converted on Cu-based catalysts.[4] Despite tremendous efforts, there is a huge debate regarding the active site of the CZA catalyst, not least because of the disparity between experimental characterization setups and industrial conditions. It was once accepted that metallic Cu serves as the active site while ZnO acts as a support,[5] although, apparently, the synergy between Cu and Zn components is critical to this technology. Several hypotheses have been further proposed to rationalize the synergy effects, including Cu$^+$ in the ZnO lattice,[6] lattice strain,[7] Schottky junctions,[8] *etc.* However, most of these hypotheses lack clear support from the latest experimental and theoretical results. In 2012, Behrens *et al.*[9] reported the experimental evidence for the enrichment of Zn on the Cu surface using X-ray photoelectron spectroscopy (XPS) and high-resolution transmission electron microscopy (HRTEM)

methods. Since then, researchers focused on two models of active sites: the CuZn surface alloy model,[10] in which Zn is reduced to form a CuZn alloy phase, and the ZnO$_x$/Cu interface model,[11] which grows *in situ* due to the strong metal–support interaction (SMSI) effect.

In addition to the fundamental efforts to clarify the reaction mechanism on the CZA catalyst, the exploration of the possibility to apply Cu single-atom catalysts (SACs) as low-temperature CO_2 hydrogenation catalysts is mainstream in heterogeneous catalysis.[12,13] The Cu SACs refer to catalysts with Cu cations stabilized by the support material, where the valence state of Cu can be tuned by the coordination environment and thus depends on the synthetic routes. Recent literature shows that these Cu SACs can exhibit distinctive product selectivity due to the delicately designed Cu coordination environment.

Another active research direction relates to the alloying between Cu and the second metal element, for example, the bimetallic Cu–M system (M = Pd,[14] Ni,[15] Fe,[16–18] *etc.*). Introducing a second metal into the Cu-catalyst can result in the formation of non-methanol products, such as methane,[15] long-chain hydrocarbons,[18] or ethanol.[16] For example, the Cu–Ni catalyst can lead to high selectivity on CH_4,[15] while the Cu–Fe catalyst tends to produce long-chain hydrocarbons.[17] However, the active site and reaction mechanism of these new catalytic systems are much less studied—whether the alloy metal is indeed the active site remains skeptical. As pointed out by Hwang *et al.*[16] in the Cu–Fe catalyst, although the CuFe alloy phase is regarded as the active site for the Cu–Fe bimetallic catalyst, FeO$_x$ and FeC$_x$ also exist in the catalyst and thus may still be the active centers.

With encouraging progress in Cu-based catalysts for CO_2 hydrogenation achieved in recent years, we here aim to overview the current understanding of the active sites of different types of Cu-based catalysts, with a particular emphasis on the atomic structure as revealed by joint theoretical calculations and experimental characterization. This Perspective is organized as follows. The thermodynamics and reaction networks for CO_2 hydrogenation are first summarized. This follows sequentially the recent advancements in probing the catalytic active sites using advanced theoretical and experimental techniques, including CZA catalysts, Cu SAC catalysts, and their closely related supported Cu cluster catalysts, and bimetallic Cu–M catalysts. Finally, an outlook for future research directions is provided.

Zhi-Pan Liu graduated in Chemistry at Shanghai Jiao Tong University (Shanghai, China). He received his PhD degree in 2003 at the Queens University of Belfast under the supervision of Prof. Peijun Hu. He then moved to the University of Cambridge, where he joined the surface science group supervised by Prof. Sir David King. In 2005 he joined Fudan University, where he has since stayed, with a position of a Changjiang professor in Physical Chemistry. His current research interests include methodology development for potential energy surface exploration, theory on heterogeneous catalysis, and machine-learning-based atomic simulation.
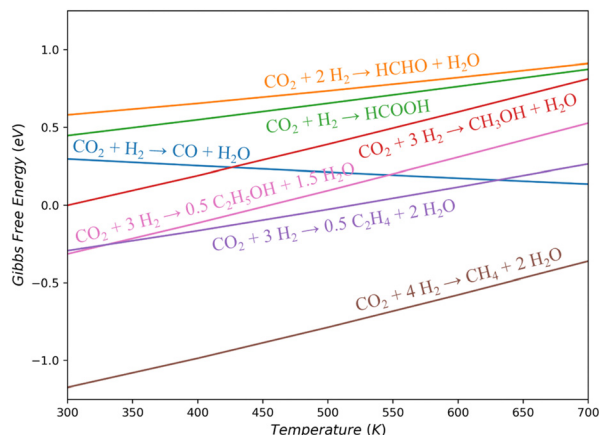
Zhi-Pan Liu

2. Thermodynamics and the kinetics of CO_2 hydrogenation on Cu surfaces

CO_2 hydrogenation can in principle yield a diverse range of products, including primary reduction products (such as CO, HCOOH, and HCHO), alcohols (CH_3OH and C_2H_5OH), and hydrocarbons (CH_4, C_2H_4, and even long-chain alkanes). It is noteworthy that while methanol is a commonly targeted product in industrial CO_2 hydrogenation, it is not the most thermodynamically favorable product at a typical operating temperature of 500 K. Fig. 1 illustrates the Gibbs free energy

Fig. 1 Gas-phase Gibbs free energy variation against temperature for CO_2 hydrogenation to low-carbon products. All gas pressures set to 1 bar.

changes (ΔG) for these gas-phase reactions.[19] It shows that CO and CH_3OH, the most frequently observed products, have similar ΔG at 500 K (0.21 and 0.39 eV, respectively), both slightly above zero. When the feed gas is compressed to increase the input pressure the reaction can be driven forward, resulting in a more favorable equilibrium conversion of CH_3OH compared to the economically undesirable CO. However, the maximum one-pass conversion of CH_3OH is still limited to 15–35%,[20] which can be increased by decreasing the temperature and increasing the pressure. Consequently, the methanol synthesis industry tends to favor lower reaction temperatures as long as the reaction rate remains acceptable.

Products other than CH_3OH and CO are less frequently reported on Cu-based catalysts. HCOOH and HCHO are thermodynamically unfavorable than CH_3OH across the entire temperature range (ΔG is 0.26/0.34 eV higher than that of CH_3OH at 500 K, respectively). They exhibit low selectivity, likely due to their instability and susceptibility to further hydrogenation into CH_3OH. Products like CH_4, C_2H_4, and C_2H_5OH are consistently thermodynamically more favorable than CH_3OH (ΔG is 1.18/0.42/0.30 eV lower at 500 K), but the hydrocarbon and multi-carbon

products are rarely reported in the products using Cu-based catalysts. On Cu metal, a model system, CO_2 hydrogenation only produces CO and CH_3OH.[21]

The answer to the conflict of product selectivity with thermodynamics preference lies in the reaction kinetics in catalysis. Fig. 2 summarizes the generally-regarded CO_2 hydrogenation mechanism on Cu surfaces obtained from density functional theory (DFT) studies.[22–27] Three general findings are outlined in the following.

(i) A most-mentioned CO_2 hydrogenation pathway to CH_3OH follows the sequence: CO_2* (superscript * indicates the adsorbed state) → HCOO* → HCOOH* → H_2COOH* → HCHO* → CH_3O* → CH_3OH*, termed the formate pathway.[22] The rate-determining step occurs in the first half of the reaction before CH_2O formation, involving the hydrogenation of CH_xO_2 ($x = 0–3$) species, such as CO_2 to HCOO*, HCOOH* to H_2COOH*, or H_2COOH to HCHO*. If the overall barrier for the further hydrogenation of HCOOH* and HCHO* is not higher than that for the formation of HCOO*, the reaction will show low product selectivity to HCOOH or HCHO, which is the case in most Cu surfaces. For example, the Gibbs free energy barriers on Cu(211) surfaces is 1.4 eV with the rate-determining steps (RDS) being CO_2 and HCOO* hydrogenation.[25]

(ii) Another mechanism for CO_2 to CH_3OH is the reverse water–gas shift (r-WGS) coupling with CO hydrogenation.[28] In the pathway, CO_2 is first hydrogenated to CO through CO_2* → COOH* → CO*, termed the carboxyl pathway, and then CO* is further hydrogenated to CH_3OH* through CO* → CHO* → HCHO* → CH_3O* → CH_3OH*, termed the formyl pathway. This pathway on metal Cu surfaces appears to be kinetically unfavorable compared to the formate pathway due to the higher Gibbs energy barrier of CO_2* → COOH*, e.g. >1.8 eV for Cu(111),[22] Cu(100)[23] and Cu(211).[27] Additionally, COOH* is less stable than HCOO* on Cu surfaces, leading to a lower rate of subsequent reactions.

(iii) Hydrogenation toward hydrocarbons or multi-carbon products is challenging on pure Cu catalysts, but appears to be likely on Cu-based multi-metallic catalysts such as CuFe and CuNi catalysts.[29] This is likely due to the high barrier associated
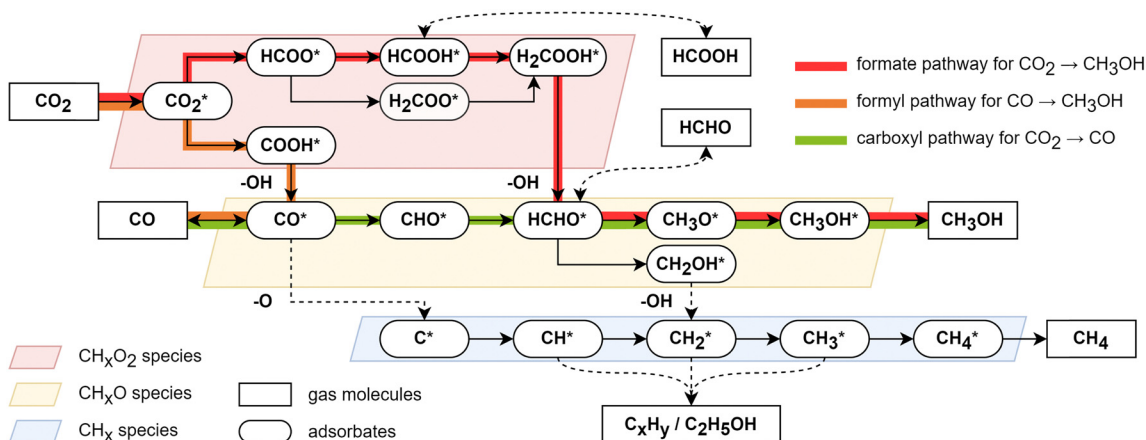

Fig. 2 The possible reaction network and reaction pathway on the Cu surface for CO_2 hydrogenations.

Table 1 The reaction and structure information of the Cu cluster and surface. E_a represents the overall barrier. RDS represents the rate determining steps

Cu surface	RDS	CN	E_a (eV)	Ref.
Cu(111)	HCOO* → H$_2$COOH*	9	1.27	22
Cu(100)	HCOO* → H$_2$COOH*	8	1.25	23
Cu(110)	HCOO* → H$_2$COOH*	7	1.19	23
Cu(111)	CO$_2$ → HCOO*	9	1.15	30
Cu(100)	CO$_2$ → HCOO*	8	1.03	30
Cu(111) point defect	CO$_2$ → HCOO*	8	1.02	30
Cu(100) point defect	CO$_2$ → HCOO*	7	0.92	30
Cu(211)	CO$_2$ → HCOO*	7	0.92	30

with the C–O bond breaking to produce CH$_x$ (x = 0–4) species, which is essential for subsequent C–C coupling.[25] The direct dissociation of CO* to form C* and O*, known to be feasible on Fe catalysts, encounters a high energy barrier (>2 eV) on Cu surfaces, making it unlikely to occur.[22] Another possible pathway of CH$_x$ generation is via the HCHO* → CH$_2$OH* → CH$_2$* route, but its overall barrier is higher than that of HCHO* → CH$_3$O* → CH$_3$OH, leading to a low selectivity.[25]

Quantitatively, the low coordination number (CN) of Cu (the number of Cu atoms neighboring the centering Cu) is generally more active in CO$_2$ hydrogenation. Table 1 summarizes the overall energy barriers on different Cu surfaces. For the same reaction step, as listed in entries 1–3, and entries 4–8 in Table 1,[22,23,30] generally the barrier is lower as long as the CN is reduced. When converting to the Gibbs free energy, the close-packed Cu(111) is found to be inert, as evidenced by the very high Gibbs free energy barrier of 1.98 eV for CO$_2$ hydrogenation, where the rate-determining step is the HCHO* + H* step.[22,25] To allow CO$_2$ hydrogenation, the introduction of step and point defects is thus a must.[25,30–32] The Cu(211) surface exhibits a significantly lower Gibbs free barrier of 1.40 eV for methanol production. These findings indicate the importance of manipulating the surface structure for enhancing the catalytic activity of Cu-based catalysts in CO$_2$ hydrogenation.

3. CZA industrial catalyst

As the active site of the CZA catalyst remains highly controversial, we first overview the basic facts of the CZA catalyst. The industrial CZA catalyst is prepared by the traditional co-precipitation method. The precipitate with a molar ratio of Cu : Zn : Al = 7 : 3 : 1 turns to composites containing at least nanoparticles (5–10 nm) of metallic Cu, wurtzite ZnO, and amorphous Al$_2$O$_3$ after air calcination and H$_2$ activation. When operated under conditions such as 500–550 K and 50–100 bar, the CZA catalyst exhibits high selectivity for methanol production (e.g., 99.8%) and exceptional long-term stability (design life >3 years).[33] It is worth noting that a mixed CO, CO$_2$, and H$_2$ feed gas, instead of pure CO$_2$ or pure CO with H$_2$, is utilized in the fixed-bed catalysis, where the CO$_2$:CO ratio range is 0.5–4.[1,34,35] Interestingly, the isotopic-labeling experiments revealed that CO$_2$ is the dominant carbon source for methanol production, accounting for more than 90% of the carbon in methanol.[24]

On the other hand, the CO-free CO$_2$/H$_2$ feed gas leads to a more oxidizing atmosphere.

There are two main vying views regarding the active sites of CZA catalysts, both of which have garnered experimental and theoretical evidence, fueling an ongoing debate. The first view posits that ZnO oxide is partially reduced and the Zn migrates to the Cu surface, leading to intermixing with the Cu lattice and the formation of a surface alloy. According to DFT calculations, the reducing potential of the feed gas is sufficient to reduce ZnO to form a CuZn surface alloy with moderate Zn coverage (0.35 ML[36] or 0.22 ML[25]), but not enough to form a CuZn bulk alloy or metallic Zn. In experiments also high content of the CuZn surface alloy is observed under strong reduction conditions, e.g., CO$_2$-free CO and H$_2$ atmospheres.[37–39] Kuld et al.[40] found an increasing Zn coverage with an increasing CO/CO$_2$ ratio in the feed gas, which led to a higher methanol reaction rate, indicating that stronger reducing potential in the feed gas resulted in higher Zn coverage. Nakamura et al.[41] also found that the maximum turnover frequency (TOF) on a Zn deposited on a Cu(111) model catalyst with 0.19 ML Zn coverage was 10 times faster compared to that on a clean Cu(111) surface. While earlier DFT studies reported that the Zn-doped Cu(211) surface shows a lower energy barrier of CO$_2$ hydrogenation to methanol than that without Zn doping, following the same formate pathway,[9,24] the later ab initio microkinetics study reveals a negative effect of Zn alloying on CO$_2$ hydrogenation activity.[42,43]

Recently, we developed a microkinetic-guided machine learning pathway search (MMLPS) method to explore the reaction network for CO$_2$ and CO hydrogenations on thermodynamically favorable Cu–Zn alloy surface structures.[25] Taking Cu(211) as an example, Fig. 3a plots 14 958 reaction pairs (IS, TS, FS) on the Cu(211) surface through automated reaction sampling based on global neural network potential (G-NN) calculations, from which the CO$_2$ and CO hydrogenation reaction pathways are resolved and the reaction mechanism is identified to be the formate pathway rather than the r-WGS pathway for CO$_2$ hydrogenation on the Cu(111) and Zn-alloyed Cu(211) surface (Fig. 3b). The key intermediates along the pathways on 0.11 ML and 0.22 ML Zn–Cu(211) surfaces are shown in Fig. 3c and d. Interestingly, we found that the Zn decorates at the step-edge of the Cu(211) surface with a coverage of up to 0.22 ML under reaction conditions, and the Zn–Zn dimeric site is thermodynamically unfavorable. CO$_2$ and CO hydrogenations occur exclusively at the step-edge of the (211) surface with a Zn coverage of up to 0.11 ML, where the low coverage of Zn (0.11 ML) does not much affect the reaction kinetics (Fig. 3b), demonstrating no activity improvement on the CuZn surface alloy. The microkinetics simulations based on DFT calculation reproduced nicely the experimental finding that CO$_2$ hydrogenation dominates methanol synthesis, instead of CO hydrogenation.

Another popular view proposes that Zn species form a ZnO$_x$(H$_y$)–Cu interface, where Zn atoms are primarily present as ZnO$_x$(H$_y$) clusters of layers on the Cu surface. It was once suggested that the reduced Zn ions migrate to the Cu surface and undergo re-oxidation, forming a few layers of ZnO$_x$ on the Cu surface and leading to an SMSI effect.[44] This phenomenon
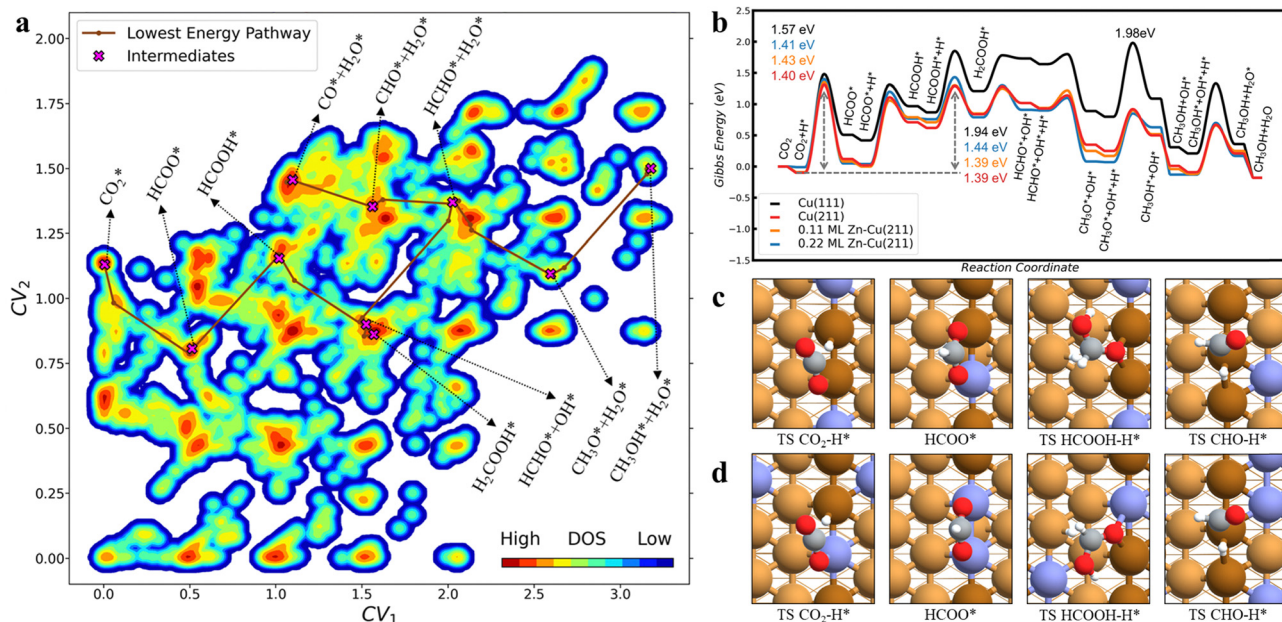
Fig. 3 (a) Contour plot for 14 958 reaction pairs (IS, TS, FS) obtained by MMLPS on the Cu(211) surface. The color indicates the occurrence frequency of the state in reaction pair collection (density of state, DOS). All structures are projected to the plot with two collective variables (CV). Key intermediates along the lowest-energy pathway are highlighted by brown lines. (b) CO_2 hydrogenation Gibbs energy profile on Cu(211) and Zn alloyed Cu(211) surfaces. (c) and (d) The structure of the key reaction step for CO_2 hydrogenation on (c) 0.11 ML Zn–Cu(211) and (d) 0.22 ML Zn–Cu(211). The color scheme for atoms is as follows: H: white; O: red; Cu: yellow; and Zn: blue. Reprinted with permission from ref. 25. Copyright 2022 American Chemical Society.

is indeed observed in HRTEM photos under *ex situ* conditions, revealing the formation of a graphite-like ZnO overlayer on the surface of Cu nanoparticles after H_2 activation (Fig. 4).[11] This phenomenon was also observed by other research groups.[9,45,46] The presence of cationic Zn as the active site was also suggested by Laudenschleger *et al.*,[47] who conducted a high-pressure pulse experiment in which NH_3 is injected into a high-pressure methanol synthesis. They observed a temporary decrease in methanol yield due to NH_3 poisoning, but the co-fed C_2H_4 hydrogenates to C_2H_6 on the Cu surface at a normal rate. Based on these observations, they proposed that a positively charged Zn on Cu is responsible for the active sites in CO_2 hydrogenation, which is poisoned by NH_3. They also reported that the higher CO_2 content, a more oxidizing condition, may lead to more positively charged Zn on the Cu surface, resulting in more obvious NH_3 poisoning.

As for the phase of Zn cations in catalysts, growing experimental and theoretical results support that the presence of H

species may be critical in the SMSI process and also in the active site, suggesting the relevance of the ZnO_xH_y phase rather than the ZnO_x phase. Beck *et al.*[36] first showed that the formation of active sites is influenced by the H_2 pressure. They observed significant changes in the Zn K-edge X-ray absorption near edge structure (XANES) signals during temperature-programmed reduction around operating temperature when the H_2 pressure was kept beyond 1 bar. However, no significant changes were observed in the zinc (+2) oxidation state until 500 °C under 1 mbar H_2. In addition, theoretical studies also found the strong adsorption of H on the ZnO_x cluster supported on Cu(111), stabilizing the ZnO_x cluster on Cu under the H_2-rich reaction conditions.[46,48–50] The presence of H may further alter the reaction kinetics. Reichenbach *et al.*[51] showed that the energy barrier of CO_2 hydrogenation on Zn_7O_3/Cu(111) is 1.33 eV, which decreases to 1.30 eV when H adsorbs on the ZnO cluster. Kattel *et al.* proposed another $Zn_6O_7H_7$/Cu(111) model whose CO_2 hydrogenation overall energy barrier is only 1.05 eV (HCOO* → H_2COOH*), much lower than that of ZnCu(211) (1.49 eV).[52] It should be noted that due to the complexity of the potential energy surface (PES), the structures of ZnO_xH_y clusters on Cu surfaces are not explored systematically yet and thus the reported energetics on the manually constructed ZnO_xH_y clusters may not be representative.

To date, it is apparent that the catalytic active site of the CZA catalyst, although still in debate, should involve low-coordinated Cu sites. The presence of Zn, as both the CuZn alloy and ZnOH are likely forms, at least helps to stabilize the active site. The advent of advanced characterization and theoretical methods has brought the understanding of active sites much closer to the truth.
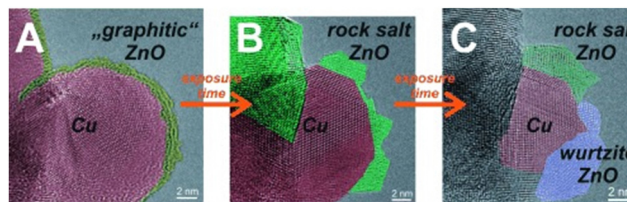

Fig. 4 (A)–(C) HRTEM images of Cu/ZnO/Al_2O_3 after different times of electron beam exposure. Red-colored sites correspond to Cu particles. Yellow indicates graphitic-like ZnO_x. Green highlights rock salt ZnO, and blue regions correspond to the wurtzite ZnO structure. Reprinted with permission from ref. 11. Copyright 2015 John Wiley & Sons, Inc.

4. Cu SACs

Cu SACs are promising low-temperature catalysts for CO_2 hydrogenation with high selectivity towards desirable products. Table 2 summarizes the recent advances in Cu SACs, highlighting the Cu coordination environment, valence state, reaction intermediates, and the computed reaction barriers, if available. As shown, three types of elements, namely O, N, and C, were explored as the anionic coordination, which can alter the valence state of Cu and also the product selectivity.

Entries 1–4 in Table 3 exhibit an interesting trend in Cu SACs, that is, methanol selectivity decreases with the increase of the Cu–O coordination number. For example, Chai et al.[13] reported 89.5% selectivity towards methanol on a faujasite-encaged mononuclear Cu center catalyst that has a higher $[CuO_{3.8}]$ coordination environment with a Cu valence state of +2 (Table 2, entry 1). Wu et al.[53] conducted a study on Cu_1/ZnO catalysts and found that CO_2 hydrogenation to methanol had a selectivity of 99.1% with Cu coordination of $[CuO_{3.5}]$ and the valence state of $Cu^{\delta+}$ ($1 < \delta < 2$) (Table 2, entry 2).

Table 2 The reaction and structure information of Cu SACs

	Cu SAC	Temp. (K)	Product (selectivity)	CN_{Cu}	$Cu^{\delta+}$	Reaction intermediates	E_a (eV)	Ref.
1	Cu_1@FAU zeolite	513	MeOH (89.5%)	$[CuO_{3.8}]$	+2	HCOO, HCOOH, CH_3O	~ 2.30	13
2	Cu_1/ZnO	443	MeOH (99.1%)	$[CuO_{3.5}]$	$1 < \delta < 2$	COOH, CH_2O	1.94	53
3	Cu_1/amorphous-ZrO_2	453	MeOH (100%)	$[CuO_3]$	+1.4	HCOO, CH_3O	1.46	12
4	Cu_1/Zr_{12}-MOF	358	EtOH (>99%)	$[CuO_3]$	+1	CHO, CH_2O, CH_3O		54
5	Cu_1/C_2N		HCOOH	$[CuN_2]$		HCOO	0.57	55
6	Cu_1/C_3N_4		HCOOH	$[CuN_4]$		HCOO	0.86	56
7	Cu_1/C_3N_4	423	CO (94.3%)	$[CuN_3]$	+1.64	COOH		57
8	Cu_1/C_3N_4	423	MeOH (95.5%)	$[CuN_4]$	+1.05	HCOO, CH_3O		57
9	Cu_1/graphine		HCOOH	$[CuC_3]$		HCOO	1.47, 1.18	58 and 59

Table 3 Catalyst composition, reaction conditions and catalytic performance of various multi-metallic catalysts for CO_2 hydrogenation. HC represents hydrocarbon

Alloy	Active site	Alloy composition	Temp (K)	Pressure (Mpa)	Conversion (%)	Product (selectivity)	Ref.
CuPd	Pd–Cu/SiO_2	Cu : Pd = 0.34 : 0.66	523	4.1	6.60	CO (66%) CH_3OH (34%)	14
	Pd–Cu/$Ti_{0.1}Zr_{0.9}O_2$	Cu : Pd =3 : 1	523	4.1	10.10	CO (55.4%) CH_3OH (44.6%)	78
	1Pd–10Cu/CeO_2	Cu : Pd = 1 : 0.06	543	3	17.8	CH_3OH (23.7%)	75
CuNi	Ni-in-Cu	Cu : Ni =4.14 : 1	673	0.1	26	CO (>99.9%)	81
	CuNi-rGO	Cu : Ni = 2 : 1	498	4.0	7.87	CH_3OH (98.7%)	82
	Cu–Ni/CeO_2-nanotubes	Cu : Ni = 2 : 1	533	4	17.8	CH_3OH (76%) CO (~ 25%)	84
	Cu–Ni/$MgAl_2O_4$	Cu : Ni = 15.5 : 1	623	—	86	CH_4 (>98%)	15
CuFe	sp-CuFeZn	Cu : Fe = 15.9 : 5.7	613	3.0	33.40	CO (18%) CH_4 (~ 14%) C_{2+} parafin (~ 49.5%) C_{2+} olefin (15.2%)	18
	im-CuFeZn	Cu : Fe = 15.7 : 5.7	613	3.0	28.60	CO (26.5%) CH_4 (~ 10%) C_{2+} paraffin (~ 10%) C_{2+} olefin (46.1%)	18
	Cs-$Cu_{0.8}Fe_{1.0}Zn_{1.0}$	Cu : Fe = 28.9 : 35.7	603	5.0	36.60	C_{2+}OH (19.8%) CO (~ 20%) C_{2+} alkane (~ 43%)	88
	4.6K–Cu–Mg–Zn–Fe	Cu : Fe = 1 : 0.98	593	5	30.40	C_{2+}OH (15.7%) CO (30.6%) C_{2+} alkane (~ 30%)	89
	Fe–Cu–K	Cu : Fe = 8.6 : 69.8	573	2.5	35	C_2–C_4 HC (~ 26%) C_{5+} HC (50.7%) C_{2+} olefin (72.7%)	16
	$CuFeO_2$-24	Cu : Fe = 1 : 1	573	1	16.70	CO (31.4%) C_{5+} HC (44.5%)	17
HEA	CoNiCuRuPd/TiO_2	Co : Ni : Cu : Ru : Pd = 1 : 1 : 1 : 1 : 1	673	0.1	~ 46	CH_4 (68.3%) CO (31.7%)	92
	$Zr_{0.5}(NiFeCuMnCo)_{0.5}O_x$	Zr : Ni : Fe : Cu : Mn : Co = 5 : 1 : 1 : 1 : 1 : 1	673	0.1	~ 29	CO (90%)	93
	$Co_3MnNiCuZnO_x$	Cu : Co : Ni = 1 : 3 : 1	773	0.1	48	CO (94%)	94

Interestingly, the study revealed that water present at the optimal levels acts as an active chemical reagent, opening the reaction pathways of $CO_2 \rightarrow COOH \rightarrow HCOOH$.

Recently, CO_2 hydrogenation to methanol with 100% selectivity was achieved on an amorphous ZrO_2 surface (Cu_1/ZrO_2) Cu SAC, as shown by Zhao and colleagues[12] (Table 2, entry 3). Not only a high selectivity, the catalyst also exhibits exceptional stability over 100 hours under 453 K reaction conditions (Fig. 5a). The authors employed in situ XANES and SSW-NN global PES exploration to identify the Cu coordination environment and found that the Cu single atom in the catalyst adopts a quasi-planar three-oxygen coordination and a valence state of +1.4, as depicted in Fig. 5b–d. Furthermore, DFT calculations prove that the amorphous ZrO_2 plays a key role in stabilizing the Cu single atom. The formation of Cu SACs is exothermic on amorphous ZrO_2 but endothermic on ZrO_2 flat (111) and terrace (112) surfaces, indicating that the amorphous ZrO_2 support is instrumental in maintaining the high stability of the Cu atom. The CO_2 hydrogenation on the isolated $Cu^{\delta+}$ cation site follows the $CO_2 \rightarrow HCOO \rightarrow H_2COO \rightarrow H_2COOH \rightarrow H_2CO \rightarrow H_3CO \rightarrow H_3COH$ pathway with the rate-determining step being the HCOO* species hydrogenation (Fig. 5e). The calculated TOF for CO_2 hydrogenation to CH_3OH on the isolated $Cu^{\delta+}$ cation is

approximately 2.89 h^{-1}, consistent with the experimental TOF of 1.37 h^{-1} and being about two orders of magnitude larger than the CO_2 hydrogenation to the CO product (0.03 h^{-1}).

By coupling neighboring [CuO$_3$], CO_2 hydrogenation can also produce ethanol with high selectivity, as shown by An et al.[54] (Table 2, entry 4). They synthesized Cu single atoms at a [CuO$_3$] coordination supported on a Zr$_{12}$ cluster in a metal–organic framework (MOF). With the assistance of a Cs$^+$ alkali cation, the catalyst exhibited >99% selectivity towards EtOH in tetrahydrofuran solution at 358 K. The proposed mechanism involved the coupling of CHO/CH$_3$O on two cooperative Cu^{1+} sites for ethanol synthesis.

Compared to the common [CuO$_x$], the [CuN$_x$] and the [CuC$_x$] patterns in Cu SACs are much less reported in the literature. The DFT calculations first reveal the low reaction barriers (<0.9 eV) for CO_2 hydrogenation to HCOOH on the [CuN$_x$] pattern (Table 2, entries 5–8).[55–59] The energy barrier on the [CuC$_x$] pattern is higher than that on the [CuN$_x$] pattern, but still lower than that on the [CuO$_x$] pattern (Table 2, entry 9).[58,59] This suggests that the [CuN$_x$] and [CuC$_x$] sites may exhibit even higher CO_2 hydrogenation activity than the [CuO$_x$] sites. Indeed, Yang et al.[57] demonstrated the high selectivity and activity of a C$_3$N$_4$-supported Cu SAC with [CuN$_4$] and [CuN$_3$] coordinations for CO_2 hydrogenation at low temperatures (<150 °C). The [CuN$_3$] site with the valence state of Cu$^{+1.64}$ tends to catalyze CO_2 hydrogenation to CO, while the [CuN$_4$] site with the valence state of Cu$^{+1.05}$ favors producing methanol via the formate pathway. This catalyst achieves a methanol selectivity of 95.5% at a CH_3OH productivity of 4.2 mmol g^{-1} h^{-1} (Table 2, entries 7 and 8), which surpasses that of the state-of-the-art CZA catalyst by 3.2 times (1 mmol g^{-1} h^{-1}). Overall, the Cu SAC exhibits excellent methanol selectivity in CO_2 hydrogenation, but the conversion rate is still too low due to the low concentration of the active site. New synthetic approaches are pursued to precisely disperse Cu single sites and inhibit the subsequent catalyst sintering.

5. Supported/confined Cu nanoclusters

Utilization of metal clusters is a common strategy to enhance the catalytic performance, not only because of the large surface area of metal particles but also due to the availability of low-coordinating surface atoms. For CO_2 hydrogenation, theoretical calculations indeed show that Cu$_4$ clusters possess a lower activation barrier of 1.18 eV for formate formation.[60] In practice, it is a major concern on how to stabilize these Cu nanoclusters to achieve long-term catalyst stability.

Various supports, such as SiO$_2$, Al$_2$O$_3$, ZrO$_2$, and CeO$_2$, have been tested and demonstrated to have good catalytic performances. Newly-formed Cu–O bonds were detected, which leads to the electron transfer between Cu and supports, giving rise to various ionic Cu species, including Cu^{2+}, Cu$^+$, and Cu$^{\delta+}$ that coexist with Cu^0 of nanoparticles. It was believed that Cu^0 is responsible for dissociating H$_2$, while Cu$^+$ polarizes the C–O
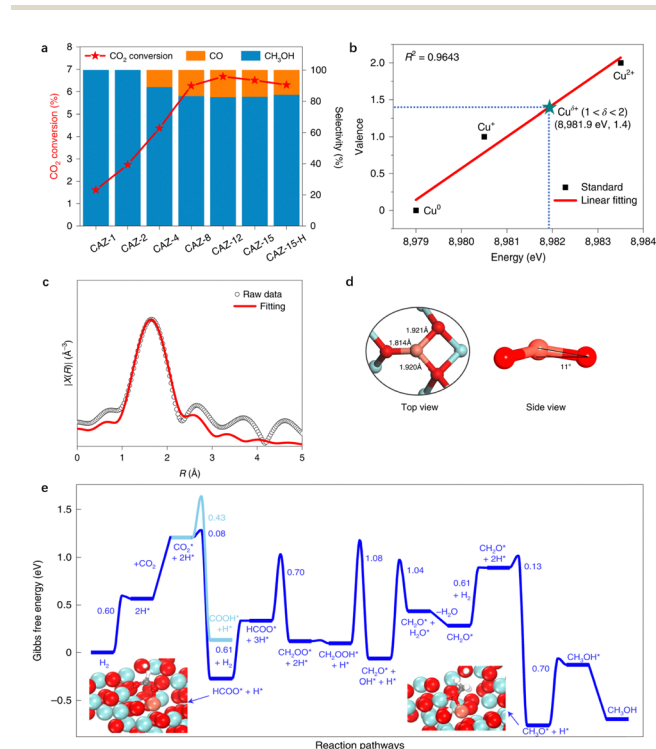

Fig. 5 The structure and catalytic performance of CO_2 hydrogenation to methanol on Cu SAC supported on the amorphous ZrO_2 surface (CAZ-1). (a) The catalytic performance of CO_2 conversion and selectivity. (b) The mean chemical valence of $Cu^{\delta+}$ species under in situ test conditions detected using XANES spectra. (c) Fitting of k^2-weighted in situ extended X-ray absorption fine structure (EXAFS) data. (d) The identified [CuO$_3$] configuration from SSW-NN simulation. (e) Gibbs free energy profile of CO_2 hydrogenation to CH_3OH/CO. Reprinted with permission from ref. 12. Copyright 2022 Springer Nature.

bond to promote intermediate conversion. The product selectivity can thus be tuned by adjusting the Cu^0/Cu^+ ratio.[61–63] For example, Yu et al.[64] demonstrated that a Cu cluster catalyst supported on inert SiO_2 prepared using flame spray pyrolysis, results in five times more Cu^+ species than the traditional catalyst made using ammonia evaporation, and increases the methanol selectivity by inhibiting CO desorption and promoting CO* hydrogenation to CH_3OH. DFT calculations by Sun et al.[65] also showed that CO adsorption on Cu^+ sites is stronger than that on Cu^0, and CO can be further hydrogenated to CHO* species.

The support may also participate in the reaction cycle by acting as the reaction site for key elementary steps. For the Cu/ ZnO catalyst, Valant et al.[66] investigated the effect of different Zn contents on CO_2 hydrogenation and found that the catalyst with Zn:(Zn + Cu) = 0.62 shows the highest methanol activity of 4.6 mol h^{-1} kg^{-1} at 523 K. The adsorbed H amount on ZnO shows a volcano-like profile against the Zn:(Zn + Cu) content, consistent with the activity variation, pointing to the synergetic effect between Cu and ZnO. Song et al. unveiled the remarkable activity (11.3%) and methanol STY (242 g_{CH_3OH} kg_{cat}^{-1} h^{-1}) of 8 wt% $Cu/ZnAl_2O_4$ at 220 °C and 3 MPa, far surpassing that of conventional 8 wt% $Cu/ZnO/Al_2O_3$ composite oxides (6.8% for CO_2 conversion and 144 g_{CH_3OH} kg_{cat}^{-1} h^{-1} for methanol yield). They believed that the $ZnAl_2O_4$ dispersed the Cu cluster with a small particle size of ~3.2 nm, quite smaller than that on ZnO/ Al_2O_3 (~6.4 nm). And the higher H_2 dissociation ability on $ZnAl_2O_4$ strongly enhanced the CO_2 conversion and methanol yield.[67] The Cu/ZrO_2 catalyst has been widely reported with high methanol yield, where ZrO_2 can facilitate the formation and transformation of formate, thereby enhancing methanol synthesis.[68–71] Especially, the crystalline phase of ZrO_2 can significantly affect the catalytic performance. As reported by Tada et al., the active sites on $Cu/a\text{-}ZrO_2$ (a: amorphous) with a TOF of 29–39 h^{-1} were more suitable for CO_2-to-methanol than those on $Cu/t\text{-}ZrO_2$ (t: tetragonal) with a TOF of 16–23 h^{-1} and $Cu/m\text{-}ZrO_2$ (m: monoclinic) with a TOF of 6–8 h^{-1}.[70]

Confining Cu nanoclusters in small cages is another approach to stabilizing nanoparticles and achieving high catalytic performance. Zhu et al. have demonstrated that the Cu nanoclusters encapsulated into MOF materials with Zr_6 oxide nodes show a high methanol yield. By subtly tuning the Zr–O–Cu interface, it is found that the Zr–O–Cu interface is at least part of the active site that strongly adsorbs CO_2. As illustrated in Fig. 6, the binding of CO_2 is not energetically favored on the Cu metal particle with slightly positive adsorption energy. The adsorption of CO_2 to the O^{2-} or $Zr^{4+}\text{-}O^{2-}$ sites of the Zr_6O_8 node to form a bidentate or tridentate carbonate is considerably stronger, resulting in adsorption energies of −42.7 and −51.0 kJ mol^{-1}, respectively. The adsorption of CO_2 at the $Cu\text{-}Zr^{4+}$ interfacial sites is significantly stronger (−80.8 kJ mol^{-1}) than the adsorption on the Cu nanoparticles and ZrO_2 nodes.[72] Cui et al. also reported a series of zeolite-fixed $Cu/ZnO_x@Na\text{-}ZSM\text{-}5$ catalysts. The ultrasmall Cu/ZnO_x nanoparticles (~2 nm) in the Na-ZSM-5 zeolite exhibit the space-time yield of methanol of 44.88 g_{MeOH} g_{Cu}^{-1} h^{-1}, much more higher than those of the supported $Cu/ZnO_x/Na\text{-}ZSM\text{-}5$ catalyst (13.32 g_{MeOH} g_{Cu}^{-1} h) and industrial $Cu/ZnO/Al_2O_3$ catalyst (8.46 g_{MeOH} g_{Cu}^{-1} h) under identical conditions. The zeolite was suggested to prevent the separation of $Cu\text{-}ZnO_x$ interfaces.[73] Ding et al. prepared a high-performance $Cu@Na\text{-}Beta$ catalyst which shows a high ethanol yield of ~14% at 300 °C ~12 000 mL g_{cat}^{-1} h^{-1}, and 2.1 MPa, corresponding to a space-time yield of ~398 mg g_{cat}^{-1} h^{-1}. They proposed the reaction key step as the reaction of CO_2* with the surface methyl species at step sites of Cu nanoparticles to form CH_3COO*, which finally leads to ethanol after the hydrogenation steps.[74]

The supported/confined Cu nanocluster offers convenient ways to access rich chemical environments of Cu, leading to low-coordination Cu, positively charged $Cu^{\delta+}$ and different interface-contacted Cu. While more adjustable variables in synthesis enable the fine tune of the catalytic performance for catalytic reactions such as CO_2 hydrogenation, it becomes increasingly difficult to resolve the catalytic active site and understand the catalytic mechanism. The higher yield and the desirable selectivity continue to be the main goals in this area of catalysis research.
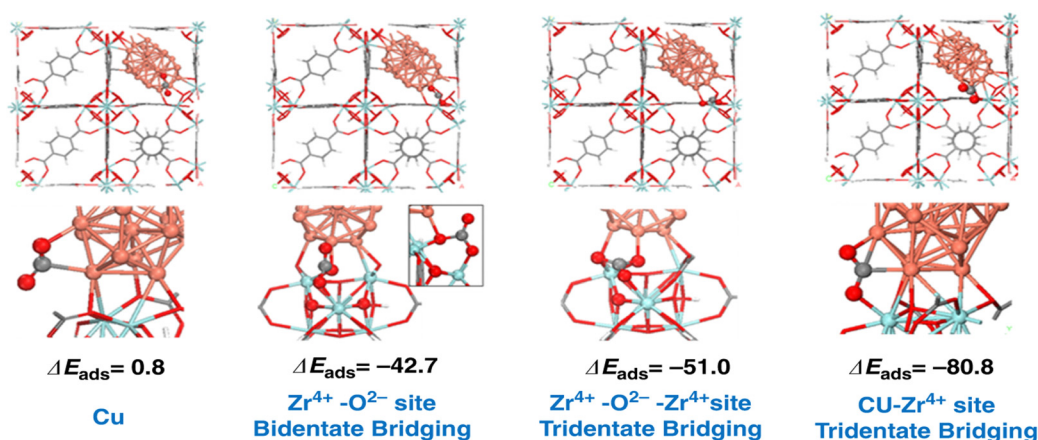

Fig. 6 Adsorption energies (ΔE_{ads} in kJ mol^{-1}) of CO_2 at different Cu/UiO-66-a interface sites. Reprinted with permission from ref. 72. Copyright 2020 Springer Nature.

6. Bimetallic Cu-based and high entropy alloy catalysts

Introducing other transition metal components into Cu can significantly modify the electronic and geometric structures of the catalyst and thus alter the catalytic performance. Table 3 summarizes the catalytic performance of representative Cu-based bimetallic catalysts and high entropy alloy (HEA) catalysts. At elevated temperatures (mostly 500–700 K) and pressures (mostly 1–5 MPa), the main products of these catalysts span a large range, including not only common CO and CH_3OH but also CH_4, long-chain hydrocarbon (HC) and even alcohols.

CO_2 hydrogenation on the Pd–Cu system produces methanol with the CO byproduct.[75] Song et al.[14,76] investigated an amorphous silica-supported Pd–Cu catalyst with a Pd/(Pd + Cu) ratio of 0.25–0.34 and found that it exhibits twice the methanol selectivity compared to the sum of the selectivities of the two corresponding monometallic catalysts. Further screening of catalyst supports led to an improved methanol selectivity of 44.6% on the Pd–Cu/$Ti_{0.1}Zr_{0.9}O_2$ catalyst.[77,78] Catalyst characterization studies by using X-ray diffraction (XRD) and TEM confirm the formation of a Pd–Cu alloy nanoparticle comprising bcc PdCu and fcc $PdCu_3$ phases.[14] Nie et al.[79] suggested that the catalytically active site is the bcc PdCu(111) surface with unsaturated Pd, as shown in Fig. 7a. The reaction proceeds through a water-assisted formate pathway with an overall Gibbs energy barrier of 1.23 eV, which is more active than the fcc $PdCu_3(111)$ surface. Microkinetics simulations show that CO formation from CO_2 through the r-WGS pathway is faster than CH_3OH synthesis, consistent with the experimental results of a high CO selectivity (>70%).

Cu–Ni alloys can catalyze CO_2 hydrogenation to CO,[80,81] CH_4,[15] or CH_3OH.[82–86] Originally, monometallic Ni is known as an active CO_2 methanation catalyst. Wang et al.[81] demonstrated that a Cu–Ni catalyst synthesized through a hydrothermal method (with a Cu/Ni ratio of 4.14) exhibits a high selectivity (>99.9%) for CO production during the r-WGS reaction at 1 bar pressure, due to the high dispersion of Ni on the Cu–Ni alloy as detected by high angle annular dark-field scanning transmission

electron microscopy (HAADF-STEM). Indeed, DFT calculations confirmed that the H-assisted CO_2 dissociation has a lower energy barrier of 1.30 eV on Ni-doped Cu(111) compared with plain Cu(111). Tan et al.[84,86] synthesized a Cu–Ni alloy on CeO_2-nanotubes and achieved CO_2 hydrogenation to CH_3OH with a maximum CH_3OH space-time yield at a Cu:Ni ratio of 2 and a CH_3OH selectivity of 76%. Summa et al.[15] used a Cu promoted Ni–Mg–Al hydrotalcite-derived catalyst with a low loading of 1.4 wt% for CO_2 hydrogenation to methane, achieving selectivity above 98% and CO_2 conversion up to 86%. XRD and XANES suggest the formation of the Cu–Ni alloy during the reduction step. Furthermore, compared with the Cu-free catalyst, promotion with Cu strongly increased the number of medium-strength basic sites revealed by CO_2 temperature programmed desorption, which is crucial for methanation.

Catalysts with Cu and Fe can lead to a distribution of multicarbon products in CO_2 hydrogenation. Fe alone serves as a famous Fischer–Tropsch catalyst that converts CO to hydrocarbon, and its combination with Cu allows direct conversion of CO_2 to a multi-carbon product.[17,87–89] Their product and selectivity are listed in Table 3. For example, Si et al.[18] developed an FeCu nanoalloy catalyst supported on ZnO by a sputtering method (sp-CuFeZn), which demonstrated a high paraffin selectivity of 63.5% (containing ∼14% of CH_4). In situ XRD reveals that in sp-CuFeZn the metal mainly exists as an $FeCu_4$ nanoalloy under the reaction conditions. Hwang et al.[16] synthesized an Fe–Cu–K catalyst that exhibited superior selectivity towards liquid hydrocarbons (50.7% toward C_{5+} hydrocarbons and 72.7% toward olefin), with a 1.7-fold increase in CO_2 conversion and higher chain growth probability compared to the Fe–K catalyst. The observed phases include the Cu–Fe alloy, Fe_3O_4, and a small amount of iron carbide (Fe_5C_2) after the reaction.

Theoretical calculations have been utilized to provide insights into the activity of the Cu–Fe alloy. Nie et al.[90,91] utilized Fe(100) and Cu-alloyed Fe(100) to investigate the reaction mechanism of CO_2 hydrogenation towards C_1 and C_2 hydrocarbons. On the Cu-alloyed Fe(100) surface, the adsorption strength of CO_2 decreases as the surface Cu coverage increases, increasing the CO_2 dissociation barrier.[91] At medium Cu coverage (θ_{Cu} = 0.4 ML), the CO_2 hydrogenation to HCOO* occurs with a low hydrogenation
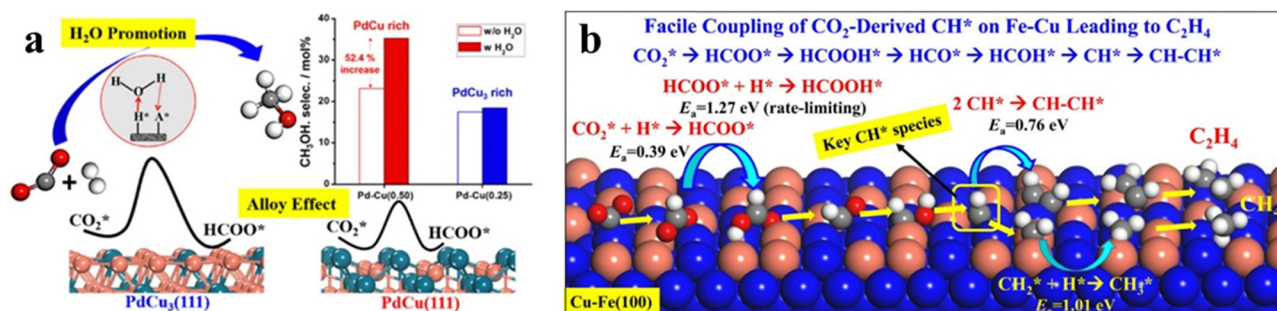

Fig. 7 (a) Methanol selectivity of different Pd–Cu bimetallic catalysts with and without H_2O. The in situ produced water can accelerate CO_2 conversion to methanol. The stepped bcc PdCu(111) active site shows a lower barrier than fcc $PdCu_3(111)$ and shows higher methanol selectivity. Reprinted with permission from ref. 79. Copyright 2018 American Chemical Society. (b) Cu-alloyed Fe(100) active sites for the Cu–Fe bimetallic catalyst and its reaction mechanism of CO_2 hydrogenation toward C_2H_4. Reprinted with permission from ref. 90. Copyright 2017 American Chemical Society.

barrier of 0.39 eV. The HCOO* species then undergoes a series of steps, including HCOO* → HCOOH* → HCO* → HCOH* → CH* → CHCH* → CH$_2$CH* → CH$_2$CH$_2$*, to produce ethylene with a low energy barrier of 1.27 eV (Fig. 7b).[90] Since these theoretical studies generally utilize single-crystal surfaces, the active site of Cu–Fe catalysts requires further detailed characterization.

While HEA emerges as a new direction in catalysis, several Cu-based HEA catalysts have also been developed for CO$_2$ hydrogenation. Mori et al.[92] synthesised a TiO$_2$ supported CoN-iCuRuPd nanoparticle catalyst, which is found to be both active and extremely durable during CO$_2$ hydrogenation. The main product leads to CH$_4$ (selectivity 68.3%) and CO (31.7%) at 673K, 1 bar with a conversion of $\sim$46%, which retained 96% of its original activity after 72 h. Hou et al.[93] reported a high entropy cubic Zr$_{0.5}$(NiFeCuMnCo)$_{0.5}$O$_x$, where the configuration entropy leads to observation of in situ reversible exsolution–dissolution of supported metallic species in multi redox cycles. In CO$_2$ hydrogenation, the CO$_2$ conversion is 29% and CO selectivity is over 90%, with no obvious activity loss during the 500 h reaction, affording ultrahigh thermal stability. It is worth noting that although the HEA catalysts do not show the desirable selectivity to high-value products (other than CO and CH$_4$), their ultrahigh thermal stability in long-term CO$_2$ hydrogenation may provide useful hints to improve catalyst durability in general. As experimental reports of HEA's applications in CO$_2$ hydrogenation are limited, more research work is needed to identify how Cu cooperates with other metals during the HEA catalysis.[92,94]

In general, Cu-based multi-metallic alloys feature the ability of making diverse products, but the activity and selectivity are still not satisfactory to meet the requirement of the industrial application. To optimize the catalyst performance, more fundamental research studies are required for probing the active site structure and resolving the reaction intermediates during CO$_2$ hydrogenation.

7. Perspectives

This perspective provides an overview of the current understanding of active sites in copper-based catalysts for CO$_2$ hydrogenation, including commercial CZA, Cu SACs, supported/confined Cu clusters, and Cu-based alloy catalysts. Generally speaking, despite the variation of the valence state and the coordination environment of Cu, the CO$_2$ hydrogenation main product of a mono-metallic Cu catalyst, e.g. CZA, Cu SACs and supported/confined Cu clusters, is either CO or methanol. Once the second metal is introduced to form a Cu–X alloy catalyst, the CO$_2$ hydrogenation product can switch to long-chain hydrocarbons such as alkanes and olefins. Therefore, how to improve the catalysts' selectivity and long-term stability is a general concern in research, which requires a deep understanding of the active sites and reaction mechanisms. There are still many challenges in the field and are highlighted as follows.

The SMSI effect observed during CZA catalyst activation is long believed to be the key reason for creating the active site and resulting in a high activity of the CZA catalyst. There is

growing interest in the in situ atomic structure of ZnO$_x$H$_y$ on Cu surfaces. As mentioned in Section 3, the traditional techniques of structure characterization face great difficulties due to the essentiality of reaction conditions (H$_2$/CO pressure) and the great complexity of the potential energy surface.

The state-of-the-art machine-learning atomic simulations emerge as a promising approach to determining the overlayer structure. Recently, we utilized the G-NN potential based grand canonical global search method, namely automatic search of optimal phase[95] (ASOP) to explore the stable Zn$_x$O$_y$H$_z$/Cu(111) structure.[25] Fig. 8a and b plot the PES of Zn$_x$O$_y$H$_z$/Cu(111) under typical reaction conditions (500 K, p_{H_2} = 40 bar, p_{CO} = p_{CO_2} = 10 bar), where the x- and y-axes are the coverage of O and Zn/H and the contour is the free energy of the minimum from G-NN. The figure contains 1751 minimum structures at different periodic supercells of Cu(111) (n_{cell} = 4–12) with varied Zn$_x$O$_y$H$_z$ composition ($\theta_{Zn} = x/n_{cell}$ = 0–1, the same for θ_O and θ_H). This shows that besides clean Cu and CuZn surface alloys (where $\theta_O \approx 0$), a stable region is located where the coverage is $\theta_{Zn} : \theta_O : \theta_H \approx 1:1:1$. After further validation by DFT for low-lying minima, a number of energetically nearly degenerate most stable structures are identified. The most stable one (GM) is (Zn$_6$O$_8$H$_8$/Cu(111) − (2$\sqrt{3}$ × 3),) whose free energy is −0.043 eV per Cu(111) unit cell, being more stable than clean Cu(111) and bulk ZnO. Many other structures with a similar energy are available, including Zn$_6$O$_8$H$_8$/Cu(111) − ($\sqrt{19}$ × $\sqrt{7}$) (denoted as I, free energy −0.038 eV per unit cell), Zn$_4$O$_5$H$_5$/Cu(111) − (3 × $\sqrt{7}$) (denoted as II, free energy −0.029 eV per unit cell), as well as Zn$_3$O$_3$H$_3$/Cu(111) − ($\sqrt{13}$ × $\sqrt{3}$) (−0.042 eV per unit cell). Apparently, these structures share a similar [–Zn–OH–Zn–] repeating unit and the multiple degenerate structures suggest the amorphous nature of the ZnO$_x$H$_y$ overlayer on the Cu(111) surface (Fig. 8c). Further work is required to clarify the ZnO$_x$H$_y$ structures on the
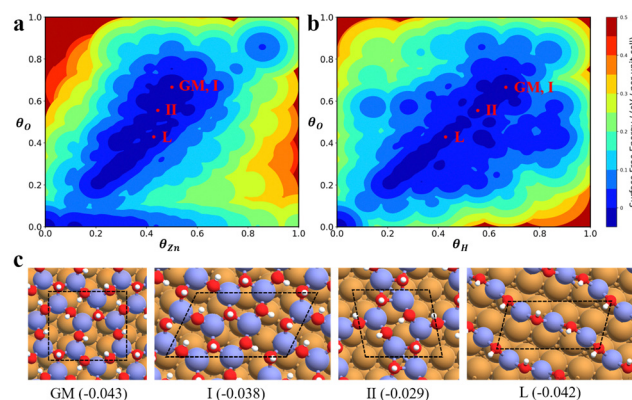

Fig. 8 The PES contour map for Zn$_x$O$_y$H$_z$/Cu(111) from ASOP simulation, using (a) coverage of O and Zn as axes, or (b) coverage of O and H as the axes. (c) The identified stable Zn$_x$O$_y$H$_z$/Cu(111) structures. From left to right, GM: Zn$_6$O$_8$H$_8$/Cu(111) − (2$\sqrt{3}$ × 3), I: Zn$_6$O$_8$H$_8$/Cu(111) − ($\sqrt{19}$ × $\sqrt{7}$), II: Zn$_4$O$_5$H$_5$/Cu(111) − (3 × $\sqrt{7}$), L: Zn$_3$O$_3$H$_3$/Cu(111) − ($\sqrt{13}$ × $\sqrt{3}$). The color scheme for atoms is as follows: H: white; O: red; Cu: yellow; and Zn: blue.

stepped Cu surfaces and determine the CO_2 hydrogenation mechanism over these overlayer structures.

In addition, the role of the Al_2O_3 component in the CZA catalyst needs to be revisited. While Al_2O_3 was traditionally viewed as a support material, it may still act as an active component in methanol synthesis. In particular, the presence of the $ZnAl_2O_4$ spinel has been mentioned in recent literature as a factor for promoting CO hydrogenation.[96,97]

For the Cu SAC catalyst, the low conversion rate (for example, $<2\%$[12,53]) limits its practical applications, which calls for increasing the metal loading and the concentration of active Cu SAC sites. Moreover, as the $[CuN_x]$ active sites have shown lower reaction barriers, it is fascinating to increase the concentration of $[CuN_x]$ active sites by immobilizing Cu SACs on nitrides such as GaN or Ta_2N_3, which may achieve better catalysis performance for CO_2 hydrogenation than $[CuO_x]$ and $[CuC_x]$ active sites.

For the supported/confined Cu cluster catalyst, optimizing the Cu-oxide interface is an effective approach to improving the activity of CO_2 hydrogenation. Recent studies have shown that the inverse oxide/metal configuration can enhance interfacial reactivity in well-defined $CeO_x/Cu(111)$, $ZnO/Cu(111)$, and ZrO_x/Cu models used as catalysts for the water–gas shift and methanol synthesis reactions.[98–100] In these models, the oxide species are grown as a thin layer on top of the copper surface, creating an interface that promotes catalytic activity by improving the electron transfer and adsorption of CO_2 and H_2 molecules. The active site structures for these inverse catalysts are however unclear.

Overcoming the above challenges in the future should benefit greatly from the rapid progress of machine learning methodology and artificial intelligence (AI) applications to catalysis. First, machine learning atomic simulations that can speed up significantly the complex PES exploration are powerful new tools to identify unknown structures,[72] and to search for unknown reactions,[25,101] as practiced by our group using SSW-NN simulations in recent years. By combining these two features of SSW-NN, it is possible to resolve the active site centers using first principles. Second, machine learning techniques hold great promise to guide the design of new materials/catalysts. A high-throughput screening scheme can be built *via* a machine learning database of materials with essential catalytic properties and then utilized to predict the activity. Recent years have seen efforts to establish a database for key catalytic properties,[102] such as the adsorption energy of key intermediates, the morphology and acidity of zeolites.[103] These approaches can be applied in the design of HEA (Cu, Co, Ni, Zn, and Sn) catalysts for CO_2 hydrogenation.[104,105]

We note that electrochemical CO_2 hydrogenation has attracted more and more attention in recent years, which is not the focus of the current perspective, and there has been significant and interesting progress. For example, the electrochemical C–N coupling of CO_2 and nitrogenous small molecules (*e.g.* NO and NO_2) can simultaneously eliminate greenhouse gas emissions and environmental pollutants;[106] the CO_2 electrochemical reduction on Cu-based catalysts can produce other high-value products (*e.g.* ethylene or ethanol) under ambient conditions.[107,108] These new reaction routes together with the thermal approach of CO_2 hydrogenation are going to be the key catalysis hotspots towards greener and more sustainable future.

Conflicts of interest

The authors declare no competing financial interests.

Acknowledgements

References

1 ICI LTD, *UK Pat.*, GB1159035A, 1969.
2 ICI LTD, *US Pat.*, US3326956A, 1967.
3 Global methanol production 2022, https://www.statista.com/statistics/1323406/methanol-production-worldwide/, (accessed 25 June 2023).
4 G. Ertl and D. R. Burgess, *Handbook of heterogeneous catalysis*, VCH, Weinheim, 1997, p. 1856.
5 K. C. Waugh, *Catal. Today*, 1992, **15**, 51–75.
6 K. Klier, in *Advances in Catalysis*, ed. D. D. Eley, H. Pines and P. B. Weisz, Academic Press, 1982, vol. 31, pp. 243–313.
7 M. M. Günter, T. Ressler, B. Bems, C. Büscher, T. Genger, O. Hinrichsen, M. Muhler and R. Schlögl, *Catal. Lett.*, 2001, **71**, 37–44.
8 J. C. Frost, *Nature*, 1988, **334**, 577–580.
9 M. Behrens, F. Studt, I. Kasatkin, S. Kuhl, M. Havecker, F. Abild-Pedersen, S. Zander, F. Girgsdies, P. Kurr, B.-L. Kniep, M. Tovar, R. W. Fischer, J. K. Norskov and R. Schlogl, *Science*, 2012, **336**, 893–897.
10 T. Fujitani, I. Nakamura, T. Uchijima and J. Nakamura, *Surf. Sci.*, 1997, **383**, 285–298.
11 T. Lunkenbein, J. Schumann, M. Behrens, R. Schlögl and M. G. Willinger, *Angew. Chem., Int. Ed.*, 2015, **54**, 4544–4548.
12 H. Zhao, R. Yu, S. Ma, K. Xu, Y. Chen, K. Jiang, Y. Fang, C. Zhu, X. Liu, Y. Tang, L. Wu, Y. Wu, Q. Jiang, P. He, Z. Liu and L. Tan, *Nat. Catal.*, 2022, **5**, 818–831.
13 Y. Chai, B. Qin, B. Li, W. Dai, G. Wu, N. Guan and L. Li, *Natl. Sci. Rev.*, 2023, **10**, nwad043.
14 X. Jiang, N. Koizumi, X. Guo and C. Song, *Appl. Catal., B*, 2015, **170–171**, 173–185.
15 P. Summa, B. Samojeden, M. Motak, D. Wierzbicki, I. Alxneit, K. Świerczek and P. Da Costa, *Catal. Today*, 2022, **384–386**, 133–145.
16 S.-M. Hwang, S. J. Han, J. E. Min, H.-G. Park, K.-W. Jun and S. K. Kim, *J. CO2 Util.*, 2019, **34**, 522–532.

17 Y. H. Choi, Y. J. Jang, H. Park, W. Y. Kim, Y. H. Lee, S. H. Choi and J. S. Lee, *Appl. Catal., B*, 2017, **202**, 605–610.

18 Z. Si, C. C. Amoo, Y. Han, J. Wei, J. Yu, Q. Ge and J. Sun, *J. Energy Chem.*, 2022, **70**, 162–173.

19 D. R. Burgess Jr., in *NIST Chemistry WebBook, NIST Standard Reference Database Number 69*, ed. P. J. Linstrom and W. G. Mallard, National Institute of Standards and Technology, Gaithersburg MD, 2021.

20 J. Zhong, X. Yang, Z. Wu, B. Liang, Y. Huang and T. Zhang, *Chem. Soc. Rev.*, 2020, **49**, 1385–1413.

21 J. Yoshihara and C. T. Campbell, *J. Catal.*, 1996, **161**, 776–782.

22 L. C. Grabow and M. Mavrikakis, *ACS Catal.*, 2011, **1**, 365–384.

23 M. D. Higham, M. G. Quesne and C. R. A. Catlow, *Dalton Trans.*, 2020, **49**, 8478–8497.

24 F. Studt, M. Behrens, E. L. Kunkes, N. Thomas, S. Zander, A. Tarasov, J. Schumann, E. Frei, J. B. Varley, F. Abild-Pedersen, J. K. Nørskov and R. Schlögl, *ChemCatChem*, 2015, **7**, 1105–1111.

25 Y.-F. Shi, P.-L. Kang, C. Shang and Z.-P. Liu, *J. Am. Chem. Soc.*, 2022, **144**, 13401–13414.

26 P. Wu and B. Yang, *ACS Catal.*, 2017, **7**, 7187–7195.

27 X. Sun, P. Wang, Z. Shao, X. Cao and P. Hu, *Sci. China: Chem.*, 2019, **62**, 1686–1697.

28 Y. Yang, D. Mei, C. H. F. Peden, C. T. Campbell and C. A. Mims, *ACS Catal.*, 2015, **5**, 7328–7337.

29 F. Zeng, C. Mebrahtu, X. Xi, L. Liao, J. Ren, J. Xie, H. J. Heeres and R. Palkovits, *Appl. Catal., B*, 2021, **291**, 120073.

30 L. Ma, W. Zhao, B. Wang, L. Ling and R. Zhang, *Fuel*, 2022, **313**, 122686.

31 W. Liao and P. Liu, *ACS Catal.*, 2020, **10**, 5723–5733.

32 X. Zhang, J. X. Liu, B. Zijlstra, I. A. W. Filot, Z. Y. Zhou, S. G. Sun and E. J. M. Hensen, *Nano Energy*, 2018, **43**, 200–209.

33 D. Sheldon, *Johns. Matthey Technol. Rev.*, 2017, **61**, 172–182.

34 S. S. Iyer, T. Renganathan, S. Pushpavanam, M. Vasudeva Kumar and N. Kaisare, *J. CO2 Util.*, 2015, **10**, 95–104.

35 K. Girod, H. Lohmann, S. Schlüter and S. Kaluza, *Processes*, 2020, **8**, 1673.

36 S. Kuld, M. Thorhauge, H. Falsig, C. F. Elkjaer, S. Helveg, I. Chorkendorff and J. Sehested, *Science*, 2016, **352**, 969–974.

37 P. Amann, B. Klötzer, D. Degerman, N. Köpfle, T. Götsch, P. Lömker, C. Rameshan, K. Ploner, D. Bikaljevic, H.-Y. Wang, M. Soldemo, M. Shipilin, C. M. Goodwin, J. Gladh, J. Halldin Stenlid, M. Börner, C. Schlueter and A. Nilsson, *Science*, 2022, **376**, 603–608.

38 A. Beck, M. Zabilskiy, M. A. Newton, O. Safonova, M. G. Willinger and J. A. van Bokhoven, *Nat. Catal.*, 2021, **4**, 488–497.

39 R. Dalebout, L. Barberis, G. Totarella, S. J. Turner, C. La Fontaine, F. M. F. de Groot, X. Carrier, A. M. J. van der Eerden, F. Meirer and P. E. de Jongh, *ACS Catal.*, 2022, **12**, 6628–6639.

40 S. Kuld, C. Conradsen, P. G. Moses, I. Chorkendorff and J. Sehested, *Angew. Chem.*, 2014, **126**, 6051–6055.

41 J. Nakamura, Y. Choi and T. Fujitani, *Top. Catal.*, 2003, **22**, 277–285.

42 S. Wang, M. Jian, H. Su and W. Li, *Chin. J. Chem. Phys.*, 2018, **31**, 284–290.

43 W. Janse van Rensburg, M. A. Petersen, M. S. Datt, J.-A. van den Berg and P. van Helden, *Catal. Lett.*, 2015, **145**, 559–568.

44 S. J. Tauster, S. C. Fung and R. L. Garten, *J. Am. Chem. Soc.*, 1978, **100**, 170–175.

45 T. Lunkenbein, F. Girgsdies, T. Kandemir, N. Thomas, M. Behrens, R. Schlögl and E. Frei, *Angew. Chem.*, 2016, **128**, 12900–12904.

46 D. Li, F. Xu, X. Tang, S. Dai, T. Pu, X. Liu, P. Tian, F. Xuan, Z. Xu, I. E. Wachs and M. Zhu, *Nat. Catal.*, 2022, **5**, 99–108.

47 D. Laudenschleger, H. Ruland and M. Muhler, *Nat. Commun.*, 2020, **11**, 3898.

48 Y. Xu, Z. Dai, Y. Ding and L. Zhang, *J. Chem. Phys.*, 2022, **157**, 221101.

49 K. Mondal, Megha, A. Banerjee, A. Fortunelli, M. Walter and M. Moseler, *J. Phys. Chem. C*, 2022, **126**, 764–771.

50 X.-K. Wu, G.-J. Xia, Z. Huang, D. K. Rai, H. Zhao, J. Zhang, J. Yun and Y.-G. Wang, *Appl. Surf. Sci.*, 2020, **525**, 146481.

51 T. Reichenbach, K. Mondal, M. Jäger, T. Vent-Schmidt, D. Himmel, V. Dybbert, A. Bruix, I. Krossing, M. Walter and M. Moseler, *J. Catal.*, 2018, **360**, 168–174.

52 S. Kattel, P. J. Ramírez, J. G. Chen, J. A. Rodriguez and P. Liu, *Science*, 2017, **355**, 1296–1299.

53 W. Wu, Y. Wang, L. Luo, M. Wang, Z. Li, Y. Chen, Z. Wang, J. Chai, Z. Cen, Y. Shi, J. Zhao, J. Zeng and H. Li, *Angew. Chem., Int. Ed.*, 2022, **61**, e202213024.

54 B. An, Z. Li, Y. Song, J. Zhang, L. Zeng, C. Wang and W. Lin, *Nat. Catal.*, 2019, **2**, 709–717.

55 J. Ma, H. Gong, T. Zhang, H. Yu, R. Zhang, Z. Liu, G. Yang, H. Sun, S. Tang and Y. Qiu, *Appl. Surf. Sci.*, 2019, **488**, 1–9.

56 K. Homlamai, T. Maihom, S. Choomwattana, M. Sawangphruk and J. Limtrakul, *Appl. Surf. Sci.*, 2020, **499**, 143928.

57 T. Yang, X. Mao, Y. Zhang, X. Wu, L. Wang, M. Chu, C.-W. Pao, S. Yang, Y. Xu and X. Huang, *Nat. Commun.*, 2021, **12**, 6022.

58 D. N. Sredojević, Ž. Šljivančanin, E. N. Brothers and M. R. Belić, *ChemistrySelect*, 2018, **3**, 2631–2637.

59 S. Ali, R. Iqbal, A. Khan, S. U. Rehman, M. Haneef and L. C. Yin, *ACS Appl. Nano Mater.*, 2021, **4**, 6893–6902.

60 C. Liu, B. Yang, E. Tyo, S. Seifert, J. DeBartolo, B. von Issendorff, P. Zapol, S. Vajda and L. A. Curtiss, *J. Am. Chem. Soc.*, 2015, **137**, 8676–8679.

61 J. Zhang, X. Sun, C. Wu, W. Hang, X. Hu, D. Qiao and B. Yan, *J. Energy Chem.*, 2023, **77**, 45–53.

62 Y. Gu, C. Han, J. Huang, V. A. Vinokurov and W. Huang, *Fuel*, 2022, **322**, 124111.

63 J. Yang, N. Gong, L. Wang, Y. Wu, T. Zhang, H. Xie, G. Yang and Y. Tan, *New J. Chem.*, 2021, **45**, 20832–20839.

64 J. F. Yu, M. Yang, J. X. Zhang, Q. J. Ge, A. Zimina, T. Pruessmann, L. Zheng, J. D. Grunwaldt and J. Sun, *ACS Catal.*, 2020, **10**, 14694–14706.

65 L. Sun, J. Han, Q. Ge, X. Zhu and H. Wang, *RSC Adv.*, 2022, **12**, 19394–19401.

66 A. Le Valant, C. Comminges, C. Tisseraud, C. Canaff, L. Pinard and Y. Pouilloux, *J. Catal.*, 2015, **324**, 41–49.

67 L. Song, H. Wang, S. Wang and Z. Qu, *Appl. Catal., B*, 2023, **322**, 122137.

68 X. Guo, D. Mao, G. Lu, S. Wang and G. Wu, *J. Mol. Catal. A: Chem.*, 2011, **345**, 60–68.

69 S. Kattel, B. Yan, Y. Yang, J. G. Chen and P. Liu, *J. Am. Chem. Soc.*, 2016, **138**, 12440–12450.

70 S. Tada, S. Kayamori, T. Honma, H. Kamei, A. Nariyuki, K. Kon, T. Toyao, K. Shimizu and S. Satokawa, *ACS Catal.*, 2018, **8**, 7809–7819.

71 K. Samson, M. Śliwa, R. P. Socha, K. Góra-Marek, D. Mucha, D. Rutkowska-Zbik, J.-F. Paul, M. Ruggiero-Mikołajczyk, R. Grabowski and J. Słoczyński, *ACS Catal.*, 2014, **4**, 3730–3741.

72 Y. Zhu, J. Zheng, J. Ye, Y. Cui, K. Koh, L. Kovarik, D. M. Camaioni, J. L. Fulton, D. G. Truhlar, M. Neurock, C. J. Cramer, O. Y. Gutiérrez and J. A. Lercher, *Nat. Commun.*, 2020, **11**, 1–11.

73 W.-G. Cui, Y.-T. Li, L. Yu, H. Zhang and T.-L. Hu, *ACS Appl. Mater. Interfaces*, 2021, **13**, 18693–18703.

74 L. Ding, T. Shi, J. Gu, Y. Cui, Z. Zhang, C. Yang, T. Chen, M. Lin, P. Wang, N. Xue, L. Peng, X. Guo, Y. Zhu, Z. Chen and W. Ding, *Chem*, 2020, **6**, 2673–2689.

75 E. J. Choi, Y. H. Lee, D.-W. Lee, D.-J. Moon and K.-Y. Lee, *Mol. Catal.*, 2017, **434**, 146–153.

76 X. Jiang, X. Wang, X. Nie, N. Koizumi, X. Guo and C. Song, *Catal. Today*, 2018, **316**, 62–70.

77 F. Lin, X. Jiang, N. Boreriboon, Z. Wang, C. Song and K. Cen, *Appl. Catal., A*, 2019, **585**, 117210.

78 F. Lin, X. Jiang, N. Boreriboon, C. Song, Z. Wang and K. Cen, *Catal. Today*, 2021, **371**, 150–161.

79 X. Nie, X. Jiang, H. Wang, W. Luo, M. J. Janik, Y. Chen, X. Guo and C. Song, *ACS Catal.*, 2018, **8**, 4873–4892.

80 K. P. Reddy, D. Kim, S. Hong, K.-J. Kim, R. Ryoo and J. Y. Park, *ACS Appl. Mater. Interfaces*, 2023, **15**, 9373–9381.

81 L.-X. Wang, E. Guan, Z. Wang, L. Wang, Z. Gong, Y. Cui, Z. Yang, C. Wang, J. Zhang, X. Meng, P. Hu, X.-Q. Gong, B. C. Gates and F.-S. Xiao, *ACS Catal.*, 2020, **10**, 9261–9270.

82 C. Wang, Y. Fang, G. Liang, X. Lv, H. Duan, Y. Li, D. Chen and M. Long, *J. CO2 Util.*, 2021, **49**, 101542.

83 F. Zhao, M. Gong, Y. Zhang and J. Li, *J. Porous Mater.*, 2016, **23**, 733–740.

84 Q. Tan, Z. Shi and D. Wu, *Ind. Eng. Chem. Res.*, 2018, **57**, 10148–10158.

85 F. Zhao, M. Gong, K. Cao, Y. Zhang, J. Li and R. Chen, *ChemCatChem*, 2017, **9**, 3772–3778.

86 Q. Tan, Z. Shi and D. Wu, *Int. J. Energy Res.*, 2019, **43**, 5392–5404.

87 J. Liu, A. Zhang, X. Jiang, M. Liu, Y. Sun, C. Song and X. Guo, *ACS Sustainable Chem. Eng.*, 2018, **6**, 10182–10190.

88 D. Xu, M. Ding, X. Hong, G. Liu and S. C. E. Tsang, *ACS Catal.*, 2020, **10**, 5250–5260.

89 D. Xu, M. Ding, X. Hong and G. Liu, *ACS Catal.*, 2020, **10**, 14516–14526.

90 X. Nie, H. Wang, M. J. Janik, Y. Chen, X. Guo and C. Song, *J. Phys. Chem. C*, 2017, **121**, 13164–13174.

91 X. Nie, H. Wang, M. J. Janik, X. Guo and C. Song, *J. Phys. Chem. C*, 2016, **120**, 9364–9373.

92 K. Mori, N. Hashimoto, N. Kamiuchi, H. Yoshida, H. Kobayashi and H. Yamashita, *Nat. Commun.*, 2021, **12**, 3884.

93 S. Hou, X. Ma, Y. Shu, J. Bao, Q. Zhang, M. Chen, P. Zhang and S. Dai, *Nat. Commun.*, 2021, **12**, 5917.

94 J. Zhao, J. Bao, S. Yang, Q. Niu, R. Xie, Q. Zhang, M. Chen, P. Zhang and S. Dai, *ACS Catal.*, 2021, **11**, 12247–12257.

95 D. Chen, C. Shang and Z.-P. Liu, *J. Chem. Phys.*, 2022, **156**, 094104.

96 J. Su, L. Zhang, H. Zhou, Y. Ye, X. Zheng, C. Liu, S. Liu, W. Jiao, X. Liu, C. Wang, Y. Wang and Z. Xie, *ACS Catal.*, 2023, **13**, 2472–2481.

97 W.-D. Hu, C.-M. Wang, Y.-D. Wang, J. Ke, G. Yang, Y.-J. Du and W.-M. Yang, *Appl. Surf. Sci.*, 2021, **569**, 151064.

98 J. A. Rodriguez, J. Graciani, J. Evans, J. B. Park, F. Yang, D. Stacchiola, S. D. Senanayake, S. Ma, M. Pérez, P. Liu, J. F. Sanz and J. Hrbek, *Angew. Chem., Int. Ed.*, 2009, **48**, 8047–8050.

99 S. D. Senanayake, D. Stacchiola and J. A. Rodriguez, *Acc. Chem. Res.*, 2013, **46**, 1702–1711.

100 C. Wu, L. Lin, J. Liu, J. Zhang, F. Zhang, T. Zhou, N. Rui, S. Yao, Y. Deng, F. Yang, W. Xu, J. Luo, Y. Zhao, B. Yan, X.-D. Wen, J. A. Rodriguez and D. Ma, *Nat. Commun.*, 2020, **11**, 5767.

101 P.-L. Kang, C. Shang and Z.-P. Liu, *J. Am. Chem. Soc.*, 2019, **141**, 20525–20536.

102 A. Kolluru, M. Shuaibi, A. Palizhati, N. Shoghi, A. Das, B. Wood, C. L. Zitnick, J. R. Kitchin and Z. W. Ulissi, *ACS Catal.*, 2022, **12**, 8572–8581.

103 S. Ma and Z.-P. Liu, *Chem. Sci.*, 2022, **13**, 5055–5068.

104 D. Roy, S. C. Mandal and B. Pathak, *J. Phys. Chem. Lett.*, 2022, **13**, 5991–6002.

105 D. Roy, S. C. Mandal and B. Pathak, *ACS Appl. Mater. Interfaces*, 2021, **13**, 56151–56163.

106 X. Peng, L. Zeng, D. Wang, Z. Liu, Y. Li, Z. Li, B. Yang, L. Lei, L. Dai and Y. Hou, *Chem. Soc. Rev.*, 2023, **52**, 2193–2237.

107 A. J. Garza, A. T. Bell and M. Head-Gordon, *ACS Catal.*, 2018, **8**, 1490–1499.

108 W. Lai, Y. Qiao, J. Zhang, Z. Lin and H. Huang, *Energy Environ. Sci.*, 2022, **15**, 3603–3629.